

Trend Filtered Mixture of Experts for Automated Gating of High-Frequency Flow Cytometry Data

Sangwon Hyun^{*1}, Tim Coleman^{†2}, Francois Ribalet^{‡3}, and Jacob Bien^{§2}

¹*Department of Statistics, University of California, Santa Cruz*

²*Department of Data Sciences and Operations, University of Southern California*

³*School of Oceanography, University of Washington*

April 17, 2025

Abstract

Ocean microbes are critical to both ocean ecosystems and the global climate. Flow cytometry, which measures cell optical properties in fluid samples, is routinely used in oceanographic research. Despite decades of accumulated data, identifying key microbial populations (a process known as “gating”) remains a significant analytical challenge. To address this, we focus on gating multidimensional, high-frequency flow cytometry data collected *continuously* on board oceanographic research vessels, capturing time- and space-wise variations in the dynamic ocean. Our paper proposes a novel mixture-of-experts model in which both the gating function and the experts are given by trend filtering. The model leverages two key assumptions: (1) Each snapshot of flow cytometry data is a mixture of multivariate Gaussians and (2) the parameters of these Gaussians vary smoothly over time. Our method uses regularization and a constraint to ensure smoothness and that cluster means match biologically distinct microbe types. We demonstrate, using flow cytometry data from the North Pacific Ocean, that our proposed model accurately matches human-annotated gating and corrects significant errors.

1 Introduction

Flow cytometry is a technology used to quantify the abundance of different cell populations in a fluid sample. Cells pass single file through a laser, and a vector of optical characteristics of each cell is measured, which is used to infer the cell’s subtype. While flow cytometry was originally developed for medical research, this technology was introduced to oceanography 40 years ago, leveraging the natural fluorescence of chlorophyll and other pigments within photosynthetic microbes to build valuable time-series data (Sosik et al., 2010). Oceanographic flow-cytometers, like CytoBuoy (Dubelaar et al., 1999), FlowCytoBot (Olson et al., 2003), and SeaFlow (Swalwell et al., 2011) can sample continuously, providing high-frequency data to study subtle, short-term fluctuations in microbial populations that are often missed by traditional, lower-frequency sampling methods. For instance, SeaFlow instruments have been deployed on over 100 research cruises in the last ten years, collecting data over 240,000 km in the Pacific Ocean, providing a broader and more detailed picture of microbial communities (Ribalet et al., 2019).

Extracting meaningful information from flow cytometry data requires identifying and isolating specific phytoplankton populations—a process known as “gating”—from flow-cytometry data. Traditionally, gating has relied on manual methods, with experts drawing boundaries around populations based on visual interpretations of scatter plots and prior knowledge. However, manual gating is limited by subjectivity, inefficiency, environmental variability, scalability issues, and the inability to leverage high-dimensional data across large datasets. To address the limitations of manual gating, machine learning approaches have become

^{*}shyun2@ucsc.edu

[†]tscoleman226@gmail.com

[‡]ribalet@uw.edu

[§]jbien@usc.edu

increasingly prevalent (Cheung et al., 2021). Gaussian mixture models (GMMs) have been used to probabilistically classify cells, assuming they originate from a mixture of Gaussian distributions. For time-series data, CYBERTRACK (Minoura et al., 2019) extends GMMs to model longitudinal cell population transitions and detect changes in mixture proportions. However, these methods often assume constant optical properties, which is problematic for phytoplankton, whose properties vary with environmental conditions. Also, an existing mixture-of-experts model called **flowmix** (Hyun et al., 2023), models the flow cytometry as a regression response to environmental factors. However, the most useful environmental factors are not always available in the ocean. Furthermore, their focus is in uncovering the regression relationship between the flow cytometry and changes in the environmental factors, not gating.

The focus of this paper is on the gating problem for a time series of flow cytometry data. Specifically, we would like to devise a method to partition cells into subtypes based on their optical characteristics, for data in which the subtypes’ mean optical characteristic and probabilities vary over time. Although many pre-existing methods (Aghaeepour 2010; Ge and Sealfon 2012; Quintelier et al. 2021; more broadly reviewed by Cheung et al. 2021) have been designed for traditional flow cytometry data (taken on a single fluid sample as in medical applications), these methods do not translate well to the setting of continuous flow cytometry data observed over time. We develop a method that explicitly leverages the special time-ordered structure of continuous flow cytometry data, without requiring external data such as environmental covariates. A typical research expedition takes days to weeks and can result in hundreds of millions of cells being measured. The standard gating pipeline involves a human data curator making hundreds to thousands of cell-type determinations by eye. Our method allows for the automation of that process. Doing so provides several advantages over the manual gating approach, including increased efficiency, greater consistency and reproducibility, and the ability to provide probabilistic assignments of cells to subtypes in the case of overlapping subpopulations.

To illustrate the challenge of the gating problem, the top-left panel of Figure 1 shows pseudo-synthetic data. At each time point, there are 100 data points (particles) generated from two-component mixtures of Gaussians whose parameters and relative probabilities are derived from two estimated gated cell populations—*Prochlorococcus* and *Picoeukaryotes*—from real flow cytometry data. In this synthetic example, two populations are heavily overlapping so that it is impossible to ascertain the two populations’ parameters by eye. It would be natural for a data analyst having access to a standard flow cytometry gating algorithm to consider one of two alternatives: (a) apply the algorithm to an aggregate of all cell data across all time (i.e., ignoring time information) or (b) apply the algorithm to each individual time, and then apply a matching algorithm to ensure a consistent meaning to cluster labels across time. The bottom two panels of Figure 1 show the result of applying these two natural approaches (using a Gaussian mixture model, GMM, as the base gating procedure). We can see that both approaches are inadequate, since their cluster estimates contain either too much variance or bias to be useful or interpretable.

The top-right panel of Figure 1 shows the result of applying the method that we propose in this paper, which we call **flowtrend**. We can see that it is able to estimate the true underlying model quite accurately. The key assumption made by **flowtrend** is that the data generating mechanism changes only gradually over time. Our method explicitly models the smoothly changing nature of a time series of mixtures by combining a nonparametric estimation technique with Gaussian mixture-of-experts modeling. In order to induce smoothness, we employ a trend-filtering model (Steidl et al., 2006; Kim et al., 2009; Tibshirani, 2014) on the cluster means and probabilities across time. And from the estimated Gaussian mixture models, we can assign membership probabilities to each particle, which we can use for gating the particles.

The most similar method is the **flowmix** mixture-of-experts model (Hyun et al., 2023), which connects the time points directly by assuming the means and probabilities are regression functions of environmental covariates such as salinity, temperature or nutrients. Because many covariates are smooth across time, the means and probabilities are also estimated to be gradually varying across time. The major downside of **flowmix** is that this approach requires having environmental covariates at the analyst’s disposal, which is often not the case. Our proposed **flowtrend** model will be useful in the common setting that a scientist needs to perform gating but does not have access to relevant environmental covariates or does not want to assume a functional relationship between environment and cytograms.

Another method called CYBERTRACK (Minoura et al., 2019) uses Gaussian mixtures to perform clustering for time-series flow cytometry data. However, CYBERTRACK only models the cluster probabilities π over time as a stochastic process. Crucially, CYBERTRACK does not allow for means to be different across time. Our proposed **flowtrend** model is more appropriate for marine flow cytometry, where we know

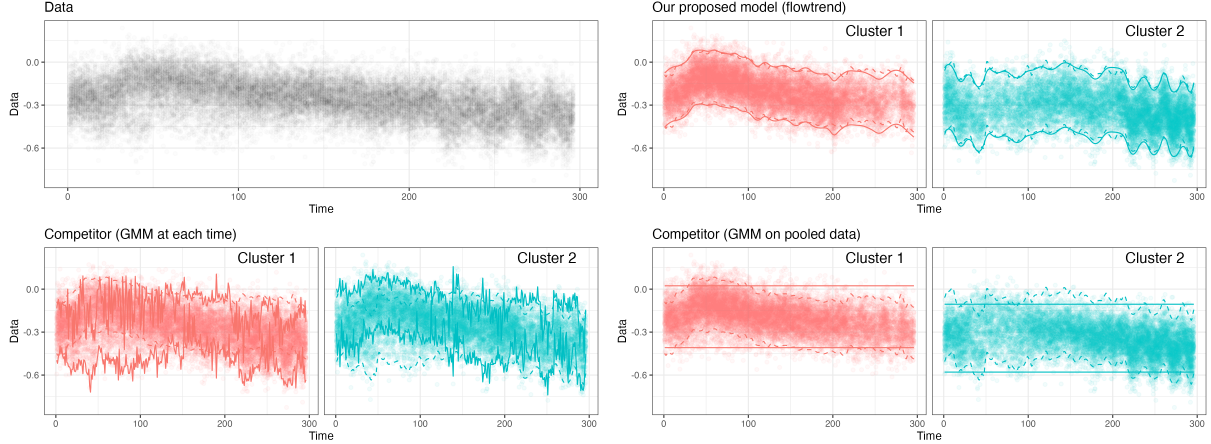


Figure 1: *The top-left shows a pseudo-synthetic data example taken from a real dataset, for illustration. Every vertical slice is a time point $t = 1, \dots, T$, and the y axis is the value of a particle in a 1-dimensional flow cytometry dataset of size $n_t = 100$ at time t . There are two Gaussian clusters at each time point, and the parameters – means and probabilities – of each cluster are changing gradually over time. This is surprisingly hard to cluster accurately, and no tools are available for this problem. The first panel shows the data as-is. The remaining three panels show the result of “gating”, or clustering the particles into two groups. The dashed lines show the true 95% probability region for each cluster, and the solid lines show each model’s estimated 95% probability region from each cluster. The **flowtrend** model closely mimics the real model. The other two GMM-based baseline models are explained in Section 3.1, and the full simulation is shown in Section 3.*

the cell populations’ optical properties shift and oscillate over time. Also, our model restricts the mean movement over time, which serves as implicit regularization of the cluster locations in their overall variation, thus allowing for a more direct biological interpretation of the estimated subpopulations.

There is a literature on mixture of regressions that is tangentially related. Wu and Yao (2016) studies a semi-parametric mixture of quantile regressions model. Huang et al. (2013) considers a nonparametric mixture of regressions, but it is only designed for a univariate response and covariate pair and, furthermore, it is not designed for repeated responses. Xiang et al. (2019) provides a comprehensive overview of semi-parametric extensions of finite mixture models. Xiang and Yao (2017) proposes a related method using single-index models. All of these methods assume that covariates accompany a univariate, non-repeated mixture responses. Our proposed method and software is explicitly designed for multivariate and repeated responses that are gradually changing across time, without the need for accompanying covariates.

Accompanying this manuscript, we also publish an R package called **flowtrend** that implements our method and is designed to work on a multi-thread high-performance parallel computing system such as SLURM Yoo et al. (2003). We used literate programming (Knuth, 1992; Bien and Vossler, 2023) to write **flowtrend**, and the supplementary materials includes a bookdown (Xie, 2016) which presents detailed explanations alongside the source code.

2 Methodology

In this section, we present our new method for modeling continuous flow cytometry data. The first three subsections introduce the three main components of the optimization problem we will be solving: the data generating model underlying our method (Section 2.1), the smoothness penalties which serve to regularize our estimates of the model parameters (Section 2.2), and the parameter constraints (Section 2.3). Section 2.4 presents an expectation-maximization algorithm based on the optimization problem. Finally Sections 2.5 and 2.6 describe how to select tuning parameters and use the model outputs in gating.

2.1 Basic model of cytogram data

The data we will model consist of an ordered sequence of d -dimensional scatterplots (which are referred to as “cytograms” hereafter). The cytogram at time t consists of data points $y_1^{(t)}, \dots, y_{n_t}^{(t)} \in \mathbb{R}^d$, corresponding to the n_t particles observed at time t . Across the T time points, there are a total of $N = \sum_{t=1}^T n_t$ points. (For applications without repeated responses, we can simply set n_t to 1.) Our model assumes that each particle $y_i^{(t)}$ has a latent cluster membership $Z_i^{(t)} \in \{1, \dots, K\}$, which will be thought of as the particle’s subtype. The K subtype relative abundances vary with time (both due to the ship’s movement and due to the passage of time): $P(Z_i^{(t)} = k) = \pi_{kt}$. Given a latent membership $Z_i^{(t)}$, we model $y_i^{(t)}$ to be distributed as

$$Y_i^{(t)} | \{Z_i^{(t)} = k\} \sim \mathcal{N}_d(\mu_{kt}, \Sigma_k).$$

Here, the vector $\mu_{kt} \in \mathbb{R}^d$ represents cell subtype k ’s mean at time t , subsetting from $\mu \in \mathbb{R}^{K \times T \times d}$. Likewise, $\Sigma_k \in \mathbb{R}^{d \times d}$ is the k ’th subtype’s variance-covariance. The choice to let the mean vary with time is based on the time-varying nature of the d optical properties being captured by flow cytometry. For example, the diameter and chlorophyll concentration of cells are known to fluctuate on a daily cycle. Also, it is reasonable to assume the shape of the distribution of a subtype, encoded in Σ_k does not change over time.

This mixture of Gaussians model has the following log-likelihood:

$$\ell(\{y_i^{(t)}\}_{i,t}; \mu, \Sigma, \pi) = -\frac{1}{N} \sum_{t=1}^T \sum_{i=1}^{n_t} \log \left[\sum_{k=1}^K \pi_{kt} \cdot \phi(y_i^{(t)}; \mu_{kt}, \Sigma_k) \right], \quad (1)$$

where Σ and π written without subscripts denote the collections of parameters $\{\Sigma_k : 1 \leq k \leq K\}$, and $\{\pi_{kt} : 1 \leq k \leq K, 1 \leq t \leq T\}$, respectively.

The particles in ocean flow cytometry data often have accompanying biomass estimates. Small particles with small biomass are likely to be more numerous than large particles. Let us call $C_i^{(t)}$ the biomass of particle $y_i^{(t)}$. To account for the relative importance that a large particle should have in the data, we reweight the log-likelihood of $y_i^{(t)}$ by a factor of $C_i^{(t)}$ so that a modified pseudo-likelihood is:

$$\ell_{\text{biomass}}(\{y_i^{(t)}\}_{i,t}, \{C_i^{(t)}\}_{i,t}; \mu, \Sigma, \pi) = -\frac{1}{N} \sum_{t=1}^T \sum_{i=1}^{n_t} C_i^{(t)} \log \left[\sum_{k=1}^K \pi_{kt} \cdot \phi(y_i^{(t)}; \mu_{kt}, \Sigma_k) \right], \quad (2)$$

where $N = \sum_{t=1}^T C_i^{(t)}$. Also, since cytograms often contain many points (with n_t as large as 100,000) computation can be challenging and compressing the data size by *binning* the particle-level cytogram data is convenient. We do this by discretizing the cytogram space into $B = D^d$ hyper-rectangles $\{E_b\}_{b=1}^B$, where D is the number of discrete values in the grid along each axis, and recording the number of particles in each grid cell at each time point t according to

$$C_b^{(t)} = \sum_{i=1}^{n_t} C_i^{(t)} \mathbb{1}(y_i^{(t)} \in E_b), \text{ for } b = 1, \dots, B; t = 1, \dots, T.$$

Let $\{y_b\}_{b=1}^B$ be the bin centers, and define $N = \sum_{b=1}^B \sum_{t=1}^T C_b^{(t)}$. From here, we can write the likelihood of the binned data,

$$\ell_{\text{binned}}(\{y_b\}_{b=1}^B, \{C_b^{(t)}\}_{b=1}^B; \mu, \Sigma, \pi) = -\frac{1}{N} \sum_{t=1}^T \sum_{b=1}^B C_b^{(t)} \log \left[\sum_{k=1}^K \pi_{kt} \cdot \phi(y_b; \mu_{kt}, \Sigma_k) \right]. \quad (3)$$

To be clear, the pseudo-likelihoods (2) and (3) are a step removed from the data generating process of the data; however, this approach is useful in practice for lessening class imbalance and making computation more feasible, and it has been used before (Hyun et al., 2023). The computational advantage of (3) is sizeable since the computation of our model depends on the number of terms in the sum of the pseudolikelihood, and in general $N \gg T \cdot B$, which in turn can be much smaller than the number of nonempty bins, $\sum_{t=1}^T \sum_{b=1}^B \mathbb{1}\{C_b^{(t)} > 0\}$. Bin sparsity leads to considerable memory savings as well: for example, for a dataset with $T = 296$

(considered in Section 4) the original particle-level data are several gigabytes whereas the binned data are in the tens of megabytes. Lastly, the expression in (2) is easily reduced to the true model when particles $y_i^{(t)}$ are observed without observation weights like biomass simply by taking $C_i^{(t)} = 1$. We use the pseudolikelihood in (2) as the basis of the objective value to optimize for the rest of the paper because it subsumes (3) as a special case.

2.2 Trend filtering of each cluster's μ and π

The basic model in Section 2.1 places no restrictions on μ_{kt} and π_{kt} , which allows them to be highly varying and choppy over time. On the other hand, it is apparent from plotting ocean flow cytometry data that the cell populations are slowly varying in time. In order to incorporate this knowledge while estimating model parameters μ_{kt} and π_{kt} , we make use of *trend filtering*, reviewed next.

Trend filtering (Steidl et al., 2006; Kim et al., 2009) is a tool for non-parametric regression on a sequence of output points $v = (v_1, \dots, v_T)$ observed at locations $x = (x_1, \dots, x_T)$. If x is equally spaced, then the l -th order trend filtering estimate is obtained by solving

$$\min_{\psi \in \mathbb{R}^T} \frac{1}{2} \|v - \psi\|_2^2 + \lambda \|D^{(l_\mu+1)} \psi\|_1,$$

where λ is a tuning parameter and $D^{(l_\mu+1)} \in \mathbb{R}^{(T-l-1) \times l}$ is the $(l_\mu + 1)$ -th order discrete differencing matrix defined recursively as $D^{(l+1)} = D^{(1)} D^{(l)}$, starting with $D^{(1)} \in \mathbb{R}^{(T-1) \times T}$:

$$D^{(1)} = \begin{bmatrix} -1 & 1 & 0 & \cdots & 0 & 0 \\ 0 & -1 & 1 & \cdots & 0 & 0 \\ \vdots & & & & & \\ 0 & 0 & 0 & \cdots & -1 & 1 \end{bmatrix}.$$

An order- l trend filtering mean estimate is a piecewise polynomial of order l . For example, $l = 0$ will produce a piecewise constant mean estimate $\hat{\mu}$. This special case is better known as the “fused lasso” (with no sparsity penalty, Tibshirani et al. 2005). Likewise, $l = 1$ will produce a piecewise linear estimate, while $l = 2$ will produce a piecewise quadratic estimate. A straightforward change in $D^{(l)}$ allows for the input x to be unevenly spaced (Tibshirani 2014, Section 6).

Porting these ideas to our problem, we add trend filtering penalties to encourage smoothness (with respect to time) in each $\mu_{k\cdot} \in \mathbb{R}^{T \times d}$ and $\pi_{k\cdot} \in \mathbb{R}^T$. For $\mu_{k\cdot}$, we use the penalty $\lambda_\mu \|D^{(l_\mu+1)} \mu_{k\cdot}\|_1$. Here, we use the notation that for a matrix M , $\|M\|_1 = \|\text{vec}(M)\|_1$. For $\pi_{k\cdot}$, we apply the penalty on the scale of logits α_{kt} (denoting the (k, t) -th entry of $\alpha \in \mathbb{R}^{K \times T}$), where

$$\pi_{kt} = \frac{\exp(\alpha_{kt})}{\sum_{m=1}^K \exp(\alpha_{mt})}. \quad (4)$$

Putting this together, we aim to minimize the following penalized negative log-likelihood:

$$-\ell_{\text{biomass}} \left(\{y_i^{(t)}\}_{i,t}, \{C_i^{(t)}\}_{i,t}; \mu, \Sigma, \pi \right) + \lambda_\mu \sum_{k=1}^K \|D^{(l_\mu+1)} \mu_{k\cdot}\|_1 + \lambda_\pi \sum_{k=1}^K \|D^{(l_\pi+1)} \alpha_{k\cdot}\|_1, \quad (5)$$

where λ_μ, λ_π are tuning parameters and l_μ, l_π are the degree of trend filtering for $\{\mu_{kt}\}_{k,t}$ and $\{\pi_{kt}\}_{k,t}$ respectively.

2.3 Restricting mean movement

It is important in our application that each mean trajectory correspond consistently across all times to the same biological cell population. While the trend filtering penalties in the previous section help encourage this behavior, we wish to enforce this more directly. Cells from the same microbial type cannot change too much over time in their characteristics, being bound by the bio-physiological limits of a single subspecies.

We therefore add to (5) an explicit constraint, requiring that all the mean vectors for cluster k across time, $\{\mu_{kt} : t = 1, \dots, T\}$, remain within a radius r of their time average $\bar{\mu}^{(k)} = 1/T \cdot \sum_{t=1}^T \mu_{kt}$:

$$\begin{aligned} \underset{\mu, \Sigma, \alpha}{\text{minimize}} \quad & -\frac{1}{N} \sum_{t=1}^T \sum_{i=1}^{n_t} C_i^{(t)} \log \left[\sum_{k=1}^K \pi_{kt} \cdot \phi \left(y_i^{(t)}; \mu_{kt}, \Sigma_k \right) \right] + \lambda_\mu \sum_{k=1}^K \|D^{(l_\mu+1)} \mu_{k\cdot}\|_1 + \lambda_\pi \sum_{k=1}^K \|D^{(l_\pi+1)} \alpha_{k\cdot}\|_1 \\ \text{subject to} \quad & \|\mu_{kt} - \bar{\mu}^{(k)}\|_2 \leq r \quad \forall t = 1, \dots, T, \text{ and } \forall k = 1, \dots, K. \end{aligned} \quad (6)$$

A similar constraint was imposed in Hyun et al. (2023) for the same reason. In contrast to λ_π and λ_μ which are tuning parameters controlling the amount of smoothness, the value of r can be reasonably pre-specified using subject matter knowledge about the variability of optical properties of cell populations of interest.

2.4 Expectation-maximization (EM) algorithm

The mixture likelihood in (6) makes this a non-convex function of μ, Σ , and π . We therefore employ an EM (Dempster et al., 1977) approach, which iteratively breaks this into simpler problems to solve. Following the standard strategy, we imagine augmenting the data with latent cluster memberships, $Z_i^{(t)}$, for each particle $y_i^{(t)}$, and write the log-likelihood ℓ_c of the *complete* data, corresponding to the joint distribution of $\{Z_i^{(t)}\}_{i,t}$ and $\{y_i^{(t)}\}_{i,t}$:

$$\ell_c \left(\{y_i^{(t)}\}_{i,t}, \{Z_i^{(t)}\}_{i,t}; \mu, \Sigma, \pi \right) = -\frac{1}{N} \sum_{t=1}^T \sum_{i=1}^{n_t} \sum_{k=1}^K \mathbb{1}(Z_i^{(t)} = k) \cdot \left[\log \pi_{kt} + \log \phi \left(y_i^{(t)}; \mu_{kt}, \Sigma_k \right) \right].$$

Because the latent cluster memberships $\{Z_i^{(t)}\}_{i,t}$ are unobservable, we integrate them out to form a surrogate objective function. For a set of parameters $\tilde{\theta} = (\tilde{\pi}, \tilde{\mu}, \tilde{\Sigma})$, we take the conditional expectation of the log-likelihood, given the observed data, $\mathbb{E}_{\tilde{\theta}}[\ell_c[\{y_i^{(t)}\}]]$, over the latent variables:

$$-\frac{1}{N} \sum_{t=1}^T \sum_{i=1}^{n_t} \sum_{k=1}^K \tilde{\gamma}_{itk} \cdot \left[\log \pi_{kt} + \log \phi \left(y_i^{(t)}; \mu_{kt}, \Sigma_k \right) \right], \quad (7)$$

where $\tilde{\gamma}_{itk} = \mathbb{E}_{\tilde{\theta}}[\mathbb{1}(Z_i^{(t)} = k) \mid y_i^{(t)}] = \mathbb{P}_{\tilde{\theta}}(Z_i^{(t)} = k \mid y_i^{(t)})$ is the conditional membership probability of particle $y_i^{(t)}$ to cluster k assuming a set of parameters $\tilde{\theta}$. These are sometimes called responsibilities in the literature, a terminology we will also adopt. We use (7) as a surrogate objective since it is easier to optimize, being convex in π and biconvex in μ and each Σ_k^{-1} . With weighted data, the surrogate (unpenalized) objective for a given parameterization $\tilde{\theta}$ is simply

$$-\frac{1}{N} \sum_{t=1}^T \sum_{i=1}^{n_t} C_i^{(t)} \sum_{k=1}^K \tilde{\gamma}_{itk} \cdot \left[\log \pi_{kt} + \log \phi \left(y_i^{(t)}; \mu_{kt}, \Sigma_k \right) \right]. \quad (8)$$

Given the latest responsibilities $\tilde{\gamma} = \{\tilde{\gamma}_{itk}\}_{i,t,k}$, we will optimize the following over μ, Σ , and π instead of solving (6):

$$\begin{aligned} Q_{\tilde{\theta}}(\mu, \Sigma, \pi) = & -\frac{1}{N} \sum_{t=1}^T \sum_{i=1}^{n_t} C_i^{(t)} \sum_{k=1}^K \tilde{\gamma}_{itk} \cdot \left[\log \pi_{kt} + \log \phi \left(y_i^{(t)}; \mu_{kt}, \Sigma_k \right) \right] + \\ & \lambda_\mu \sum_{k=1}^K \|D^{(l_\mu+1)} \mu_{k\cdot}\|_1 + \lambda_\pi \sum_{k=1}^K \|D^{(l_\pi+1)} \alpha_{k\cdot}\|_1 + \sum_{t=1}^T \sum_{k=1}^K \mathbb{1}_\infty(\|\mu_{kt} - \bar{\mu}^{(k)}\|_2 \leq r), \end{aligned} \quad (9)$$

where $\mathbb{1}_\infty\{\cdot\}$ is an infinite indicator that encodes hard constraints. We optimize a sequence of such surrogates in a penalized EM algorithm—to be described next—by alternating between the following two steps:

1. E-step: Estimate the particle responsibilities $\tilde{\gamma}$.

2. M-step: Estimate (μ, Σ, π) the parameters by maximizing the surrogate objective (9).

Prior to applying the algorithm, the initial values of the parameters are set as follows. The initial cluster means $\mu_{kt\cdot}$ are chosen to be the same for all t , i.e. $\mu_{kt\cdot} = m_k$, where $m_k \in \mathbb{R}^d$ is randomly sampled from the empirical distribution of all $\{y_i^{(t)}\}_{i,t}$ (after truncating the heights so that the high-density regions are capped). This strategy is designed to prevent initial cluster means from only being in high-density regions in the data. The cluster probabilities π_{kt} are initialized as $1/K$ for all k and t , and the covariance matrices are initialized as identity matrices of dimension $d \times d$.

Next we give details of the E- and M-steps.

E-Step

For a given set of parameters (μ, Σ, π) , we can calculate the responsibility of a particle $y_i^{(t)}$ as a ratio of weighted Gaussian density functions:

$$\tilde{\gamma}_{itk}(\mu, \Sigma, \pi) = \frac{\pi_{kt} \cdot \phi(y_i^{(t)}; \mu_{kt\cdot}, \Sigma_k)}{\sum_{j=1}^K \pi_{jt} \cdot \phi(y_i^{(t)}; \mu_{jt\cdot}, \Sigma_j)}. \quad (10)$$

M-Step

Once the responsibilities are estimated, we can derive updates for (μ, Σ, π) by optimizing (9) with respect to each parameter.

Updating μ : For fixed γ , we solve the following problem:

$$\begin{aligned} \min_{\mu \in \mathbb{R}^{d \times T \times K}} & -\frac{1}{N} \sum_{t=1}^T \sum_{i=1}^{n_t} C_i^{(t)} \sum_{k=1}^K \tilde{\gamma}_{itk} \cdot \left[\log \pi_{kt} + \log \phi(y_i^{(t)}; \mu_{kt\cdot}, \Sigma_k) \right] + \\ & \lambda_\mu \sum_{k=1}^K \|D^{(l_\mu+1)} \mu_{k\cdot\cdot}\|_1 + \sum_{t=1}^T \sum_{k=1}^K \mathbb{1}_\infty(\|\mu_{kt\cdot} - \bar{\mu}^{(k)}\|_2 \leq r). \end{aligned} \quad (11)$$

Importantly, the problem in (11) separates over k , so we can treat each cluster separately. Then, for cluster k , the problem becomes to solve,

$$\begin{aligned} \text{minimize}_{\mu_{k\cdot\cdot} \in \mathbb{R}^{T \times d}} & \frac{1}{2N} \sum_{t=1}^T \sum_{i=1}^{n_t} \tilde{\gamma}_{itk} (y_i^{(t)} - \mu_{kt\cdot})^\top \hat{\Sigma}_k^{-1} (y_i^{(t)} - \mu_{kt\cdot}) + \lambda_\mu \sum_{j=1}^d \|D^{(l_\mu+1)} \mu_{k\cdot j}\|_1 \\ \text{subject to} & \|\mu_{kt\cdot} - \bar{\mu}^{(k)}\|_2 \leq r \quad \forall t = 1, \dots, T, \end{aligned} \quad (12)$$

To solve this minimization problem, we devise an alternating direction method of multipliers (ADMM; Boyd et al. 2011) algorithm. We first reformulate (12) as follows:

$$\begin{aligned} \text{minimize}_{\mu, w, z} & \frac{1}{2N} \sum_{t=1}^T \sum_{i=1}^{n_t} \tilde{\gamma}_{itk} (y_i^{(t)} - \mu_{kt\cdot})^\top \hat{\Sigma}_k^{-1} (y_i^{(t)} - \mu_{kt\cdot}) + \lambda_\mu \sum_{j=1}^d \|D^{(1)} w_{\cdot j}\|_1 \\ \text{subject to} & \|z_t\|_2 \leq r \quad \forall t = 1, \dots, T, \\ & D^{(l_\mu)} \mu_{k\cdot j} = w_j \quad \forall j = 1, \dots, d, \\ & \mu_{kt\cdot} - \bar{\mu}^{(k)} = z_t \quad \forall t = 1, \dots, T. \end{aligned} \quad (13)$$

Note that z is in $\mathbb{R}^{T \times d}$, and $z_t \in \mathbb{R}^d$ is a column vector taken from the t -th row of z . Also, $w \in \mathbb{R}^{(T-l) \times d}$ and $w_{\cdot j}$ is a column vector taken from the j -th column of w . Then, introducing the auxillary variables

$\{u_z^{(t)} \in \mathbb{R}^d\}_{t=1}^T$ and $\{u_w^{(j)} \in \mathbb{R}^{T-l}\}_{j=1}^d$, the augmented Lagrangian is given by:

$$\begin{aligned} L(\mu_{k..}, w, z, \{u_w^{(j)}\}_1^d, \{u_z^{(t)}\}_1^T) &= \frac{1}{2N} \sum_{t=1}^T \sum_{i=1}^{n_t} \tilde{\gamma}_{itk} (y_i^{(t)} - \mu_{kt.})^\top \hat{\Sigma}_k^{-1} (y_i^{(t)} - \mu_{kt.}) \\ &+ \lambda_\mu \sum_{j=1}^d \|D^{(1)} w_{.j}\|_1 + \sum_{t=1}^T \mathbb{1}_\infty(\|z_{t.}\|_2 \leq r) \\ &+ \sum_{t=1}^T \left[u_z^{(t)\top} (\mu_{kt.} - \bar{\mu}^{(k)} - z_{t.}) + \frac{\rho}{2} \|\mu_{kt.} - \bar{\mu}^{(k)} - z_{t.}\|^2 \right] \\ &+ \sum_{j=1}^d \left[u_w^{(j)\top} (D^{(l_\mu)} \mu_{k.j} - w_{.j}) + \frac{\rho}{2} \|D^{(l_\mu)} \mu_{k.j} - w_{.j}\|^2 \right]. \end{aligned}$$

From this, we can write down the ADMM updates:

1. $\hat{\mu}_{k..} \leftarrow \operatorname{argmin}_{\mu_{k..}} L(\mu_{k..}, \hat{w}, \hat{z}, \{u_w^{(j)}\}_1^d, \{u_z^{(t)}\}_1^T)$
- 2a. $\hat{z}_t \leftarrow \operatorname{argmin}_{z_t} L(\hat{\mu}_{k..}, \hat{w}, z, \{u_w^{(j)}\}_1^d, \{u_z^{(t)}\}_1^T)$ for $t = 1, \dots, T$
- 2b. $\hat{w}_j \leftarrow \operatorname{argmin}_{w_j} L(\hat{\mu}_{k..}, w, \hat{z}, \{u_w^{(j)}\}_1^d, \{u_z^{(t)}\}_1^T)$ for $j = 1, \dots, d$
- 3a. $u_z^{(t)} \leftarrow u_z^{(t)} + \rho(\hat{\mu}_{kt.} - \bar{\mu}^{(k)} - \hat{z}_t)$ for $t = 1, \dots, T$
- 3b. $u_w^{(j)} \leftarrow u_w^{(j)} + \rho(D^{(l_\mu)} \hat{\mu}_{k.j} - \hat{w}_j)$ for $j = 1, \dots, d$.

Details for each of these ADMM updates are given in the Appendix B. A notable characteristic of our algorithm is its ability to leverage (a) existing trend filtering solvers and (b) efficient Sylvester equation solvers.

Updating π : Smooth estimation of π requires trend filtering of $\alpha_{k.} \in \mathbb{R}^T$ for each cluster k , where we recall from (4) that $\pi_{kt} = \frac{\exp(\alpha_{kt})}{\sum_{m=1}^K \exp(\alpha_{mt})}$. While trend-filtering software exists for the binomial and Poisson families (**glmgen**, Arnold et al. 2014), it does not exist for the multinomial family. We therefore re-express the minimization problem in (9) over α to a multinomial lasso problem, which we solve using **glmnet** (Friedman et al., 2022). In particular, replacing π_{kt} in (9) with the corresponding expression involving $\alpha_{k.}$, we wish to solve

$$\min_{\alpha} -\frac{1}{N} \sum_{t=1}^T \left\{ \sum_{k=1}^K \tilde{\gamma}_{tk} \alpha_{kt} - n_t \log \sum_{k=1}^K e^{\alpha_{kt}} \right\} + \lambda_\pi \sum_{k=1}^K \|D^{(l_\pi+1)} \alpha_{k.}\|_1, \quad (14)$$

where $\tilde{\gamma}_{tk} = \sum_{i=1}^{n_t} C_i^{(t)} \tilde{\gamma}_{itk}$. This is a multinomial regression with $\{\tilde{\gamma}_{tk}\}_{t,k}$ as responses and an identity design matrix, together with a trend filtering penalty on coefficients $\alpha_{k.}$. While there is not a unique minimizer in terms of α (adding a constant vector achieves the same objective value), the problem has a unique minimizer in terms of π . Using Lemma 2 from Tibshirani (2014), we transform (14) to the following ℓ_1 -penalized multinomial regression problem,

$$\min_{\omega} -\frac{1}{N} \sum_{t=1}^T \left\{ \sum_{k=1}^K \tilde{\gamma}_{tk} \omega_k^\top h_t - n_t \log \sum_{l=1}^K e^{\omega_l^\top h_t} \right\} + \frac{l_\pi!}{N^{l_\pi}} \lambda_\pi \sum_{k=1}^K \sum_{j=l_\pi+2}^T |\omega_{kj}| \quad (15)$$

where $\alpha_{kt} = h_t^\top \omega_k$, and h_t are rows of a $T \times T$ trend filtering regression matrix H defined in Appendix C. This optimization problem is an ℓ_1 -penalized multinomial regression, with no penalty on the first $l_\pi + 1$ terms. Intuitively, H consists of basis functions that are polynomials of order l_π that are 0 up until a specified point in time. We use **glmnet** to regress responses $\{\tilde{\gamma}_{tk}\}_{t,k}$ against regressors $\{h_t\}_t$ in a penalized multinomial regression.

Updating Σ : Σ is updated by a weighted empirical covariance matrix,

$$\Sigma_k \leftarrow \frac{\sum_{t=1}^T \sum_{i=1}^{n_t} C_i^{(t)} \tilde{\gamma}_{itk} (y_i^{(t)} - \mu_{kt.})(y_i^{(t)} - \mu_{kt.})^\top}{\sum_{t=1}^T \sum_{i=1}^{n_t} \tilde{\gamma}_{itk}}.$$

2.5 Prediction and cross validation

We next describe a cross validation approach for selecting the regularization parameters λ_π and λ_μ . Since the data inputs to trend filtering are a time series, we use a specialized split of the data for cross validation following the M -fold cross validation described in the `cv.trendfilter` function in the `genlasso` package (Arnold et al., 2020). Let M denote the number of data folds. Set aside the endpoints $t = 1$ and $t = T$; these are not included in any fold but are later made available to every fold for prediction. Next, every M^{th} time point starting with time point m is assigned to fold m (for $m = 1, \dots, M$), which we will call I_m . The complement is called $I_{-m} := \bigcup_{(1:M) \setminus m} I_m$. Also denote as $y_{-m} := \{y^{(t)}, t \notin I_m\}$ the data not in fold m . Then, a cross validation score is calculated via

$$CV_M(\lambda_\mu, \lambda_\pi) = \frac{1}{M} \sum_{m=1}^M \ell_{\text{biomass}}(\{y^{(t)}\}_{t \in I_m}, \{C^{(t)}\}_{t \in I_m}; \hat{\mu}^{(-m)}(I_m), \hat{\pi}^{(-m)}(I_m), \hat{\Sigma}^{(-m)}). \quad (16)$$

Here, the out-of-sample mean estimates $\hat{\mu}^{(-m)}(I_m)$ are made (a) using the estimated model $\hat{\mu}^{(-m)}(\cdot)$ from data y_{-m} , and (b) linearly interpolated at the time points I_m .

Specifically, for cluster k , in order to compute an out-of-sample mean estimate $\hat{\mu}_k^{(-m)}(\{t^*\})$ at a point $t^* \in I_m$, we first let $\lfloor t^* \rfloor$ denote the nearest t in I_{-m} less than t^* , and similarly define $\lceil t^* \rceil$. Then, we compute:

$$\hat{\mu}_k^{(-m)}(\{t^*\}) = \frac{\lfloor t^* \rfloor - t^*}{\lfloor t^* \rfloor - \lceil t^* \rceil} \hat{\mu}_k^{(-m)}(\{\lfloor t^* \rfloor\}) + \frac{t^* - \lceil t^* \rceil}{\lceil t^* \rceil - \lfloor t^* \rfloor} \hat{\mu}_k^{(-m)}(\{\lceil t^* \rceil\}). \quad (17)$$

Interpolation for π is done similarly.

With this, we choose the regularization parameters λ_μ and λ_π as the values that minimize the cross validation score $CV_M(\lambda_\mu, \lambda_\pi)$:

$$(\hat{\lambda}_\mu, \hat{\lambda}_\pi) = \underset{\lambda_\mu \in L_\mu, \lambda_\pi \in L_\pi}{\operatorname{argmin}} CV_M(\lambda_\mu, \lambda_\pi),$$

among pairs of values $(\lambda_\mu, \lambda_\pi)$ in a logarithmically spaced two-dimensional grid of values $L_\mu \times L_\pi$.

2.6 Soft gating

When gating is done manually, each particle is assigned to a single cell type. The responsibilities from (10) offer a probability vector for each particle instead:

$$\gamma_{itk}(\hat{\mu}, \hat{\Sigma}, \hat{\pi}) = \frac{\hat{\pi}_{kt} \cdot \phi(y_i^{(t)}; \hat{\mu}_{kt}, \hat{\Sigma}_k)}{\sum_{j=1}^K \hat{\pi}_{jt} \cdot \phi(y_i^{(t)}; \hat{\mu}_{jt}, \hat{\Sigma}_j)} \text{ for } k = 1, \dots, K.$$

If one wishes to assign a particle to a single cell type, we consider two approaches. A randomized strategy, which we call “soft gating” draws from this categorical probability distribution:

$$\hat{z}_i^{\text{soft}} = k \text{ with probability } \gamma_{itk}(\hat{\mu}, \hat{\Sigma}, \hat{\pi}), k = 1, \dots, K.$$

By contrast, “hard gating” is deterministic and picks the particle’s membership according to the largest responsibility:

$$\hat{z}_i^{\text{hard}} = \underset{k=1, \dots, K}{\operatorname{argmax}} \gamma_{itk}(\hat{\mu}, \hat{\Sigma}, \hat{\pi}).$$

The difference is illustrated in Figure 2, which shows soft and hard gating of the particles from simulated data at a particular time, based on an estimated `flowtrend` model. In our paper, we opt for soft gating \hat{z}_i^{soft} for gating, since the resulting gated particles resemble the estimated clusters’ distributions more closely.

3 Numerical experiments

To our knowledge, ours is the first methodology developed for the task of gating a time series of cytograms where the cluster locations and probabilities are both changing across time, without being constrained by environmental covariates. In this section, we demonstrate the performance of our method numerically. For the sake of comparison, we present two baseline procedures (and an “oracle” model) that take gating procedures designed for single cytograms and extend them to be applied to a time series of cytograms.

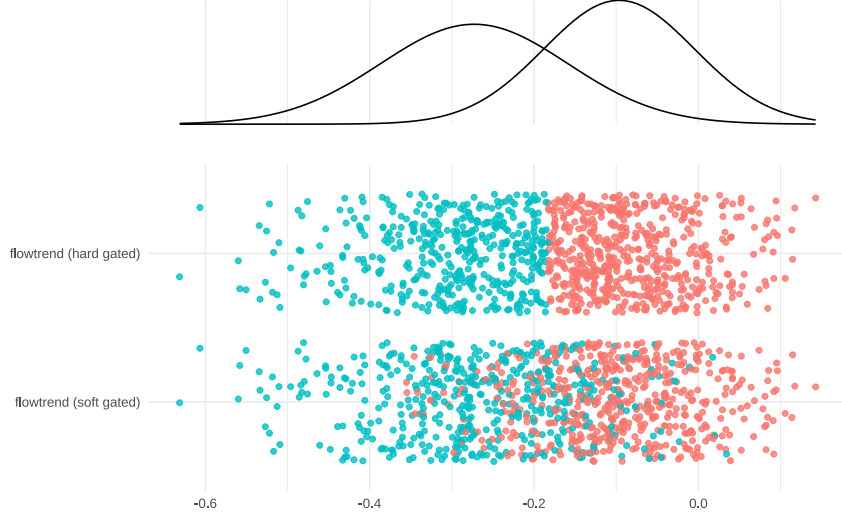


Figure 2: *Hard versus soft gating.* The data are from a particular signal size and time point ($\Delta = 2$ and $t = 60$) of simulated data, described shortly in Section 3. The $n_t = 1,000$ particles’ values are heavily overlapping, hence jittered for ease of visualization. Displayed on top are the two flowtrend-estimated Gaussian density curves of the two clusters. The colors of the points show the drawn cluster memberships from the two styles (soft and hard) of gating – described in Section 2.6.

3.1 Baselines using Gaussian mixtures

Oracle model: The oracle clusters $\{y_i^{(t)}\}_{i,t}$ by generating memberships $Z_i^{(t)}$ with full knowledge of the underlying data generating model at each time point. In other words, for each particle we make a single draw from the categorical distribution, using the true parameters (μ^*, Σ^*, π^*) :

$$\hat{Z}_i^{(t)} = k \text{ with probability } \gamma_{itk}(\mu^*, \Sigma^*, \pi^*), k = 1, \dots, K.$$

Overfit model (individual cytogram clustering): In this model, we apply a Gaussian mixture model (GMM) to each cytogram individually. This gives a separate estimate of the three parameters μ_{kt} , π_{kt} , and Σ_{kt} , the k ’th cluster mean, probability and variance at every time point t . Since the estimated cluster labels $1, \dots, K$ at any time point are arbitrary, we sequentially permute cluster labels to make them consistent across time. Specifically, in comparing a Gaussian mixture at time t and another at time $t + 1$, we first calculate all costs $\{c_{ij}; i, j = 1, \dots, K\}$ between the i -th Gaussian $F_i^{(t)}$ from one mixture model and j -th Gaussian $F_j^{(t+1)}$ of the next time point’s mixture model as a symmetrized Kullback–Leibler (KL) divergence:

$$c_{ij} = \frac{1}{2}KL(F_i^{(t)}, F_j^{(t+1)}) + \frac{1}{2}KL(F_j^{(t+1)}, F_i^{(t)}).$$

Then, we use the Hungarian algorithm (Kuhn, 1955) which uses costs $\{c_{ij}\}_{i,j}$ to find the best cluster assignment of K Gaussians at time t to those at time $t + 1$.

Underfit model (pooled cytogram clustering): For this model, we pool all the particles into a single cytogram and estimate a single Gaussian mixture model to this pooled cytogram.

These overfit and underfit models represent two plausible adaptations of existing finite mixture models for gating cytograms. They represent two opposing approaches for gating a time series of cytograms. The overfit model learns separately from each time point and uses other time points’ data only to connect cluster memberships. The underfit model ignores temporal variation when finding the two clusters in the data. We will conduct simulations to compare our **flowtrend** method to these models.

3.2 Simulation design

In order to create realistic synthetic data, we generate from two real cell populations' mixture model parameters estimated from flow cytometry data in the Gradients 2 oceanographic research cruise from the Seaflow datasets (Ribalet et al., 2019). From the estimated **flowmix** mixture of experts model on this dataset (see Hyun et al. (2023) for more detail), we isolated our attention to the cell diameter (the first of the $d = 3$ dimensions), and took two clusters representing two subpopulations of phytoplankton. The first population, according to expert annotation, is a smaller-sized *Prochlorococcus* picoplankton population, and the second population is a larger-sized *PicoEukaryote* population. The two populations' mean diameters $\{\mu_{1t1}\}_t$ and $\{\mu_{2t1}\}_t$ and log odds $\{\alpha_{1t} := \log(\pi_{1t}/\pi_{2t})\}_t$ were smoothed using trend-filtering (with degree $l = 2$ for means, $l = 1$ for $\{\gamma_{1t}\}_t$, cross-validated), to make them piecewise quadratic and piecewise linear. The smoothed γ_{1t} was further transformed back to probabilities by $\pi_{1t} = \frac{1}{1 + \exp \gamma_{1t}}$ and $\pi_{2t} = 1 - \pi_{1t}$.

Out of these two smoothed means, we kept the first cluster mean in its same place, and shifted the second cluster mean. First denote the mean of the first cluster $\mu_{1.1}^\Delta \in \mathbb{R}^T$ as equal to $\mu_{1.1}$ for all $\Delta = 0, \dots, 12$. The second cluster mean $\mu_{2.1}^\Delta$ is then defined by the offset index Δ so that the average of $\mu_{2.1}^\Delta$ is equal to that of $\mu_{1.1}$ when $\Delta = 0$, and at the other end, to be at its original position in the real estimated model when $\Delta = 12$:

$$\mu_{2.1}^\Delta = \mu_{2.1} + \frac{\Delta}{12} \cdot (\bar{\mu}_{2.1} - \bar{\mu}_{1.1}),$$

denoting as $\bar{\mu}^{(k)} = (1/T) \cdot \sum_t \mu_{kt1}$, $k = 1, 2$ the averages of each cluster mean.

For each signal size Δ , we generated n_t particles per time point, $\{y_i^{(t)}, t = 1, \dots, 296, i = 1, \dots, n_t\}$, from a mixture of Gaussians, whose latent membership $z_i^{*,(t)}$ was drawn to be k with probability π_{kt} . Conditional on membership k , the particle $y_i^{(t)}$ was generated as

$$(y_i^{(t)} | z_i^{*,(t)} = k) \sim \mathcal{N}(\mu_{.t}^\Delta, \sigma_k^2) \text{ for } k = 1, 2,$$

where $\sigma_1 = 0.0918$ and $\sigma_2 = 0.114$ were estimates taken from the estimated **flowmix** model. The resulting data are shown in the top panel of Figure 3. For a robust simulation, we repeated 10 simulations for each signal size Δ and for different sample sizes $n_t = 100, 200, 300, 400, 500$.

3.3 Simulation results

We begin by examining the overall quality of the estimation by **flowtrend** using oceanographic context. The first of the two clusters corresponds to a *Prochlorococcus* plankton population, whose true mean $\mu_{1.1}$ has a distinct and repeated daily oscillation between time points 167 through 196 (see Panel A of Figure 3). This oscillation is due to a clear cell division and photosynthesis pattern driven by the intensity of sunlight throughout a 24-hour cycle; we would hope for a good model to capture this. Indeed, our **flowtrend** model estimates this well – across all signal sizes, our method incurs a very small error in model fit.

We measure gating performance using the Rand index (Rand, 1971), which compares two partitions of a set of points by calculating the proportion of the time a pair of points are in the same set in both partitions. That is, we compare an estimated partition $\{\hat{z}_i^{(t)}\}_t$ to the true partition $\{z_i^{*,(t)}\}_{i,t}$ as

$$\text{Rand index} = \frac{\sum_{t_1, t_2 \in \{1, \dots, T\}} \sum_{1 \leq i_1 \leq n_{t_1}, 1 \leq i_2 \leq n_{t_2}, i_1 \neq i_2 \text{ if } t_1 = t_2} \mathbb{1}(\hat{z}_{i_1}^{(t_1)} = z_{i_2}^{*,(t_2)})}{\binom{N}{2} - \sum_{t=1}^T n_t}$$

We compare the clustering performance of **flowtrend** to the overfit, underfit, and oracle models described in Section 3.1.

The bottom row of Figure 3 summarizes the simulation results. For most signal sizes Δ , **flowtrend** outperforms the two baseline models (Panel B and C of Figure 3). The overfit model gates noticeably poorly compared to the underfit or **flowtrend** model; this is because the estimated models are highly varying, and the automatic matching is also poor when the signal size Δ is low. The underfit model – which has constant means, variance, and probability over t – seems to have gating performance closer to that of **flowtrend**, despite having estimated model parameters very different from the truth. This is because in our simulation example, precisely estimating the clusters' location and spread in the latter time points is

relatively unimportant for gating performance – since one of the clusters has very small probability. But we note that over all values of Δ , (i) compared to the oracle (Panel C of Figure 3) **flowtrend** does significantly better, and (ii) the estimated **flowtrend** model parameters are very close to the truth (Appendix A).

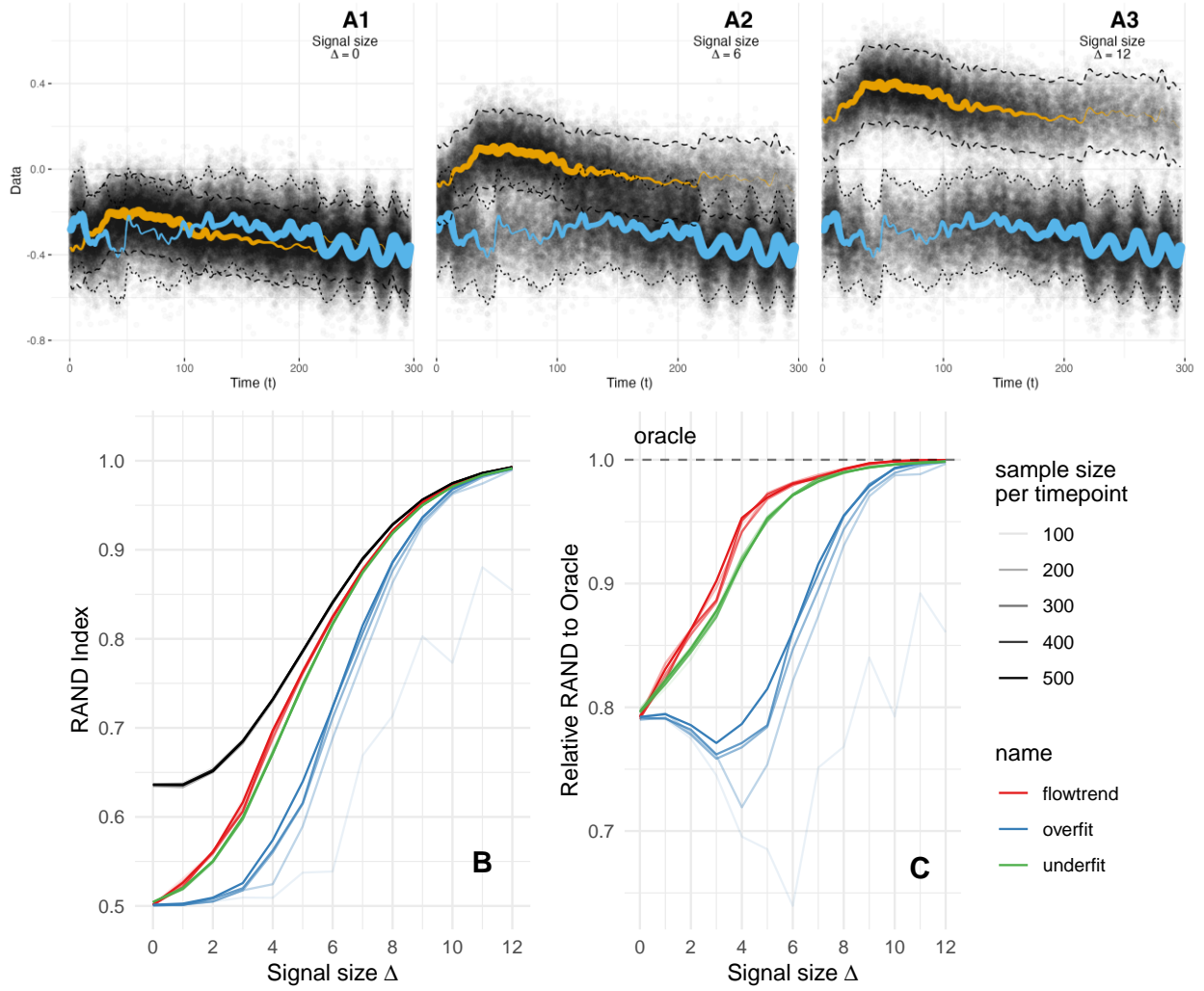


Figure 3: *Simulation data and results. Panel A1, A2 and A3 show examples of simulated data used in Section 3.3 with signal size $\Delta = 0, 6$ and 11 . In the simulation, the signal size Δ is varied from 0 (where the lower cluster mean μ_{1t1} and upper cluster mean μ_{2t1} over t are maximally overlapping) to 12 (corresponding to their original amount of separation in the real data). The two curves are smoothed cell diameter means originating from actual data, and their thickness represent cluster probabilities, which are also smoothed versions from actual data. The dotted and dashed lines show the ± 1.96 standard deviation regions around the cluster means of the two populations. In the bottom panels, the points show performance from 10 simulation repetitions at each signal size $\Delta = 0, 1, \dots, 12$. Panel B shows the Rand index of the three models in colors, and the oracle model in black. Panel C shows the relative ratio of the three models' Rand index to the oracle's Rand index.*

4 Application to Seaflo data

We apply our **flowtrend** model to the Gradients 2 cruise from the Seaflo datasets (Ribalet et al., 2019). The cytograms from this cruise are recorded almost continuously, but aggregated to each unique hour for a

total of $T = 296$ time points, and consist of $d = 3$ optical properties of the cells, as explained earlier in the paper. All original measurements (cell diameter, red fluorescence, and orange fluorescence) have been log transformed, and shifted/scaled to be between about 0 and 8.

We first perform cross validation to select tuning parameters for the **flowtrend** model, resulting in parameter estimates $\hat{\mu}$, $\hat{\Sigma}$, $\hat{\pi}$. Using these, we soft-gated the particles as described in Section 2.6. Figure 4 shows the resulting gated subpopulations of picoplankton. The cluster names come from having an expert look at the gates and annotate. The labels stand for picoplankton species such as *Prochlorococcus*, *Synechococcus*, and *PicoEukaryotes*. Our method successfully identified one subpopulation as a calibration bead, which does not change over time in cytogram space.

Panel C of Figure 4 shows the relative biomass of the estimated **flowtrend** model clusters over time (represented by $\hat{\pi}_{kt}$ for cluster k at time t). The dashed lines show the original ten π estimates in colors according to the expert-annotated microbial species. Out of the ten clusters, we will focus our attention on the clusters that correspond to known species of picophytoplankton. The thick solid lines show the sum of certain clusters corresponding to the same species – for instance, *Synechococcus* was detected as two different clusters (labeled Syn1 and Syn2 in Figure 4), and the sum of their π_{kt} at each time point represents the total estimate of *Synechococcus* over time. We can see a gradual increase of *Prochlorococcus* biomass as the cruise passes the North-Pacific transition zone. We also see a thriving of PicoEukaryotes relative to *Synechococcus* and *Prochlorococcus* in northern, cold and nutrient-rich waters. Indeed, along the north-south transect line, there are different “niches” where each of these three major subpopulations seem to thrive.

Next, we compare the gating results from **flowtrend** to what we will refer to as *traditional gating*. From the manuscript Ribalet et al. (2019) that originally processed and analyzed this data, the authors’ gating strategy is written as follows: “The classification of particles into cell populations was conducted uniformly across all samples using a combination of manual gating and unsupervised clustering algorithms,” such as **flowDensity** (Malek et al., 2014). Table 5 shows the cluster expert-annotated membership comparison, and Figure 6 visually compares all particles’ gating results at one time point. We now make some observations based on the results. It is visually clear that the traditional gating employs hard-gating while **flowtrend** uses soft-gating (as described in Section 2.6). Nonetheless, the overall agreement of the two clusterings is quite high. The bottom panel of Table 5 shows the row-normalized contingency table as a heatmap, showing that almost all ($> 90\%$) particles gated as a known major cell subspecies (abbreviated as prochloro, synecho, beads, or picoeuk) by **flowtrend** were labeled the same by traditional gating. The Rand index of all particles across all time points is about 0.7280.

If we examine the Rand index at each time point separately, we can see that the Rand is quite high before crossing the transition zone, and becomes abruptly lower after it (see Appendix A). Fewer than one-tenth of *Prochlorococcus* particles according to traditional gating are classified as unknown by **flowtrend**. This points to a mistake made by traditional gating on data directly after crossing the transition zone from north to south. However, 33% of particles that **flowtrend** deems to be *Prochlorococcus*, traditional gating calls unknown. This is caused by the traditional gating’s hard-gating strategy failing to capture *Prochlorococcus* particles that overlap with the unknown (debris) cluster. The two methods easily agree on PicoEukaryotes, since they are always located in the top-right corner of diameter-chlorophyll plots (in Figure 6). The agreement in *Synechococcus* is also strikingly high. Both agree on most ($> 95\%$) particles. This is due to *Synechococcus* being easier than *Prochlorococcus* to gate since it is clearly separable in orange fluorescence. The agreement on beads is also relatively high.

5 Discussion

In this paper, we propose a new trend-filtered mixture-of-experts model that specializes in automatic gating flow cytometry data continuously collected over time. We conducted a realistic synthetic simulation as well as a careful application to real ocean flow cytometry data collected from the North Pacific ocean. Our method gates the cells in this dataset very similarly to a human-intensive, hand-gated approach from a previous study. Doing so reveals additional insights about the niches in the North Pacific ocean observed in terms of relative abundances of major microbial species. Since there is no suitable gating method in the literature a time-series of marine flow cytometry, an automatic tool such as ours will be a valuable addition to the literature.

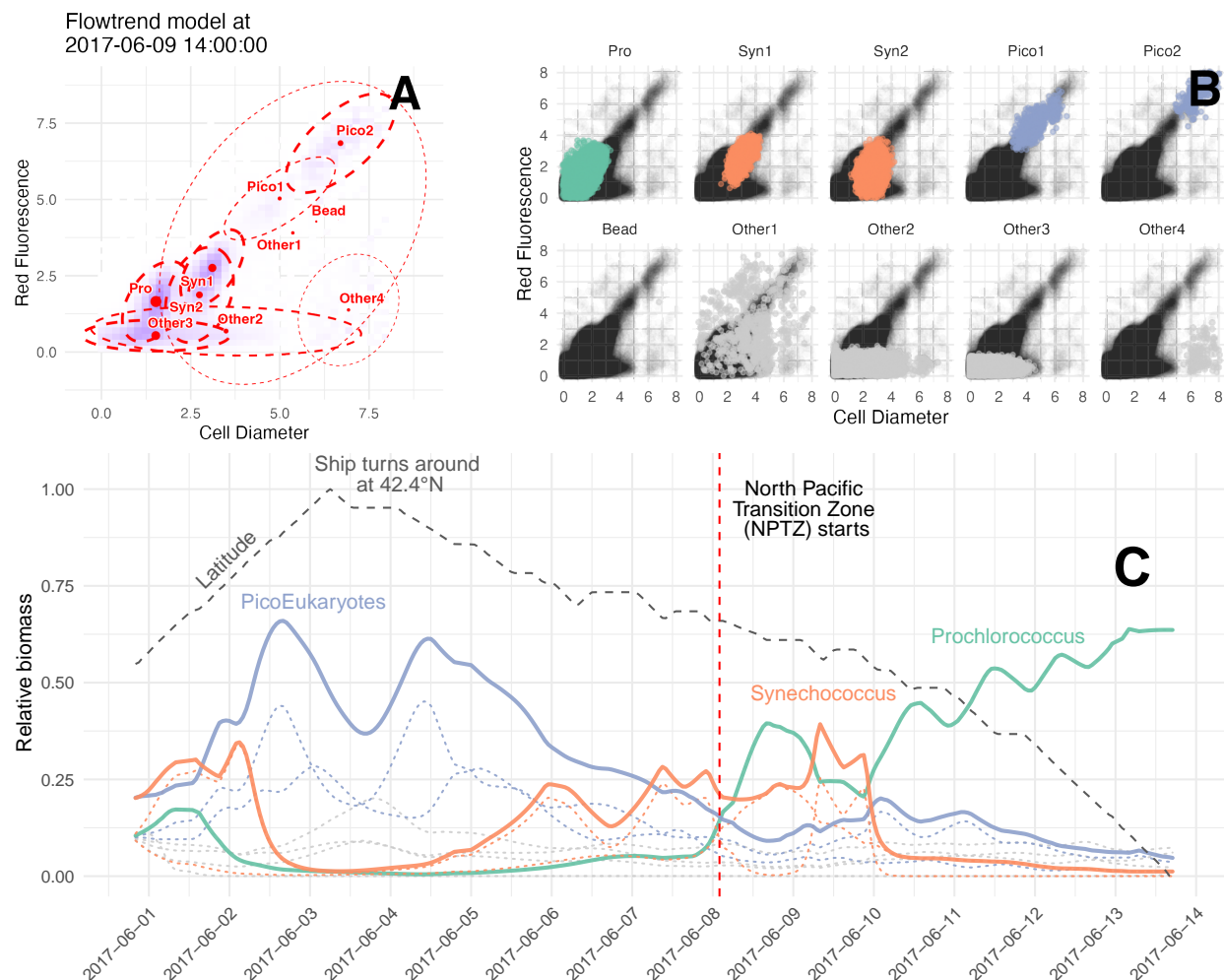


Figure 4: [Top row, panels A & B] The top row shows the estimated 10-cluster flowtrend model (Panel A) used for probabilistically classifying particles (Panel B). Out of 296 time points, only one time point (2017-06-09, at 14:00:00 UTC) is shown in these panels. Each particle is soft-gated, as described in Section 2.6 In Panel A, the estimated 95% probability ellipses are shown in dashed red lines, and the solid red circles represent the cluster means – all plotted over a backdrop showing the binned particles' distribution. In Panel B, all particles are shown in each of the ten subpanels, in transparent black points. The solid colored points mark the gated particles assigned to each cluster. The cluster labels on the panel titles are from expert annotation, and stand for major picoplankton species such as *Prochlorococcus* (Pro), *Synechococcus* (Syn1, Syn2), *PicoEukaryote* (Pico1, Pico2). [Bottom row, Panel C] The estimated relative biomass over time are shown in Panel C. Thick solid colored lines show the total relative abundance for *Prochlorococcus*, *Synechococcus* and *PicoEukaryotes*. The latter two subspecies each have two associated clusters identified by our model, whose relative abundance over time is shown in thinner dotted lines of the same color. (Grey dashed lines show the relative abundance of estimated clusters that do not clearly match with a major species).

The idea of fitting a mixture of trend filtering models is, to our knowledge, entirely novel. A problem-specific feature of our approach is the explicit constraint on the cluster means, which comes from biological understanding of phytoplankton.

Estimating the model properly requires many repeated applications of the algorithm to different slices of the data and hyperparameters. The computational cost is quite large for users without access to a parallel computing system or many CPU cores. It will be important in future work to develop a model selection

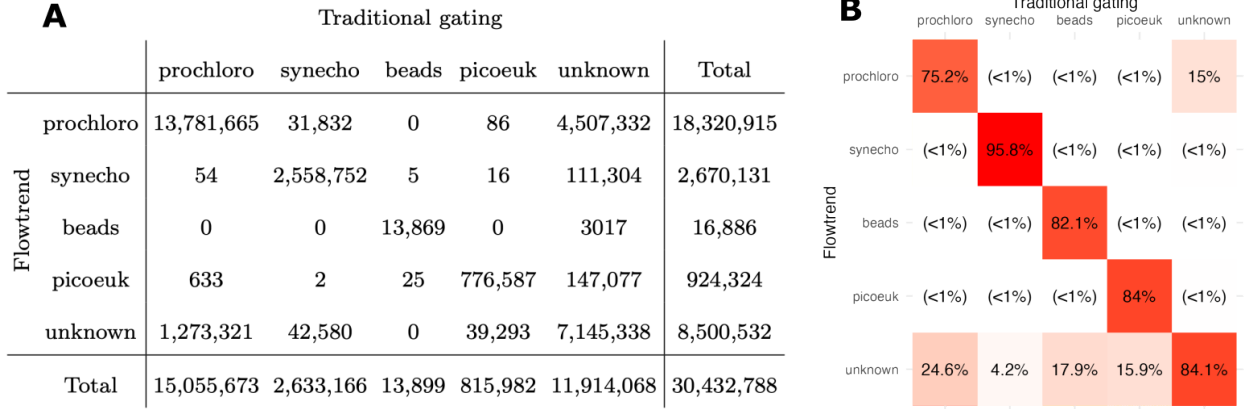


Figure 5: [Panel A] A five by five contingency table comparing **flowtrend** gating and traditional gating. Each gating method identified five major subpopulations across over 30 million particles collected on the Gradients2 cruise. The overall agreement is high (Rand Index 0.7280). [Panel B] Each row of the contingency table is scaled to sum to 100% and shown as a heatmap. For instance, the first row shows the estimated relative class frequency from traditional gating, out of the the 18,320,915 cells that **flowtrend** found to be *Prochlorococcus*. 91.54% of those cells are also found to be *Prochlorococcus* by traditional gating.

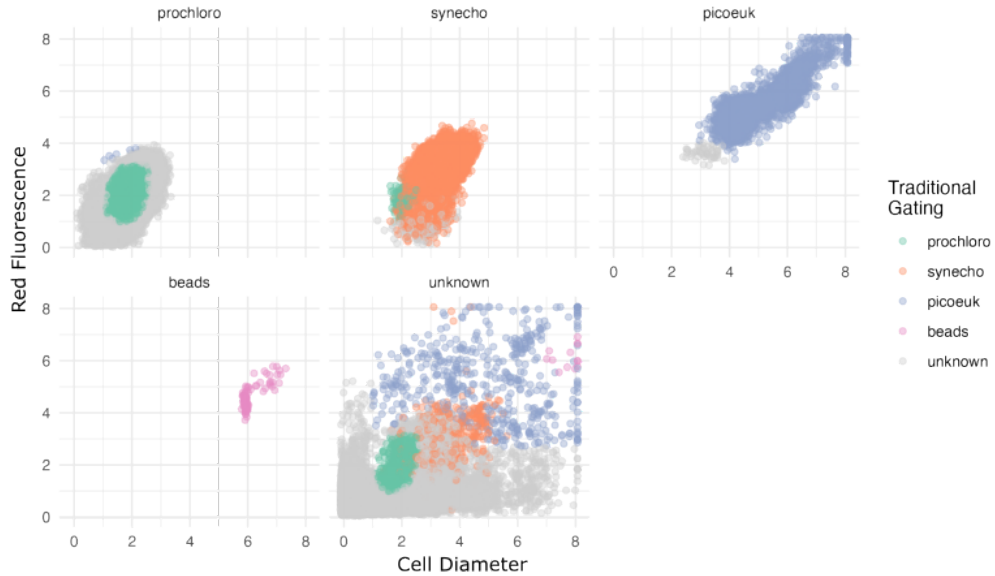


Figure 6: Gating comparison at one time point (2017-06-01, during the hour starting at 07:00:00 UTC). The same data was clustered and expert-annotated in two ways – using our **flowtrend** method, and using traditional gating (described in Ribalet et al. 2019). In each of the five panels, we show the gated major cell subpopulations of interest (*Prochlorococcus*, *Synechococcus*, *Beads*, and *PicoEukaryotes*) by **flowtrend**. In those same plots, the color of the points show the gated particles using traditional gating.

strategy (e.g. information criteria) to reduce the overall computational cost. Also, statistical inference for model parameters such as relative abundance π and membership probabilities $P(z_{it} = k \mid y_i^{(t)})$ would be valuable for scientists.

6 Acknowledgments

This work was supported by grants by the Simons Collaboration on Computational Biogeochemical Modeling of Marine Ecosystems/CBIOMES (Grant ID: 549939 to JB, Microbial Oceanography Project Award ID 574495 to FR, 1195553 to SH). We also thank Chris Berthiaume and Dr. Annette Hynes for their help in processing and curating SeaFlow data. The authors also acknowledge the Center for Advanced Research Computing (CARC) at the University of Southern California for providing computing resources that have contributed to the research results reported within this publication. URL: <https://carc.usc.edu>.

Appendix A: Additional figures

Figure 7 shows the Rand index calculated separately for cytograms at each time point.

Figure 8 and 9 show the fitted mean and probabilities for the simulation example, at several signal sizes.

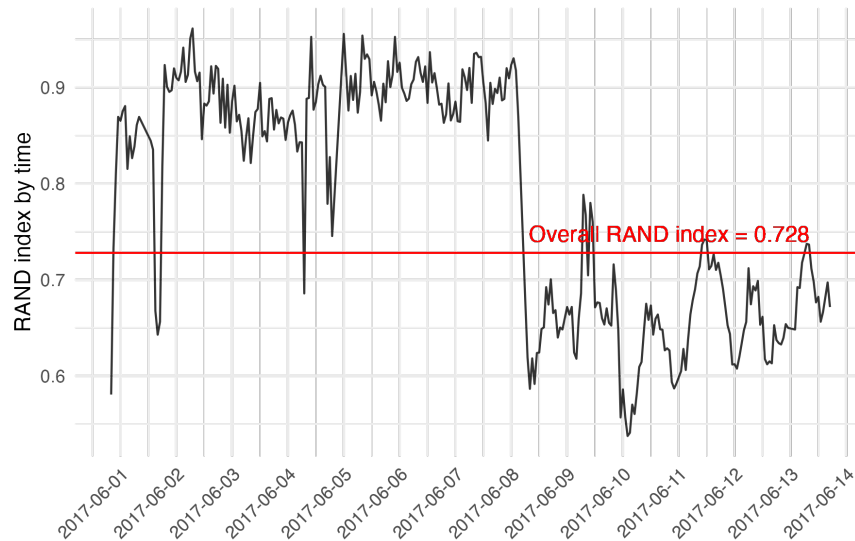


Figure 7: *Rand index calculated at each time point between flowtrend soft-gated memberships and traditional gating memberships, on real flow cytometry data described in Section 4. There is a high agreement around 0.9 before the transition zone crossing at about time point $t = 170$, and lower agreement afterwards.*

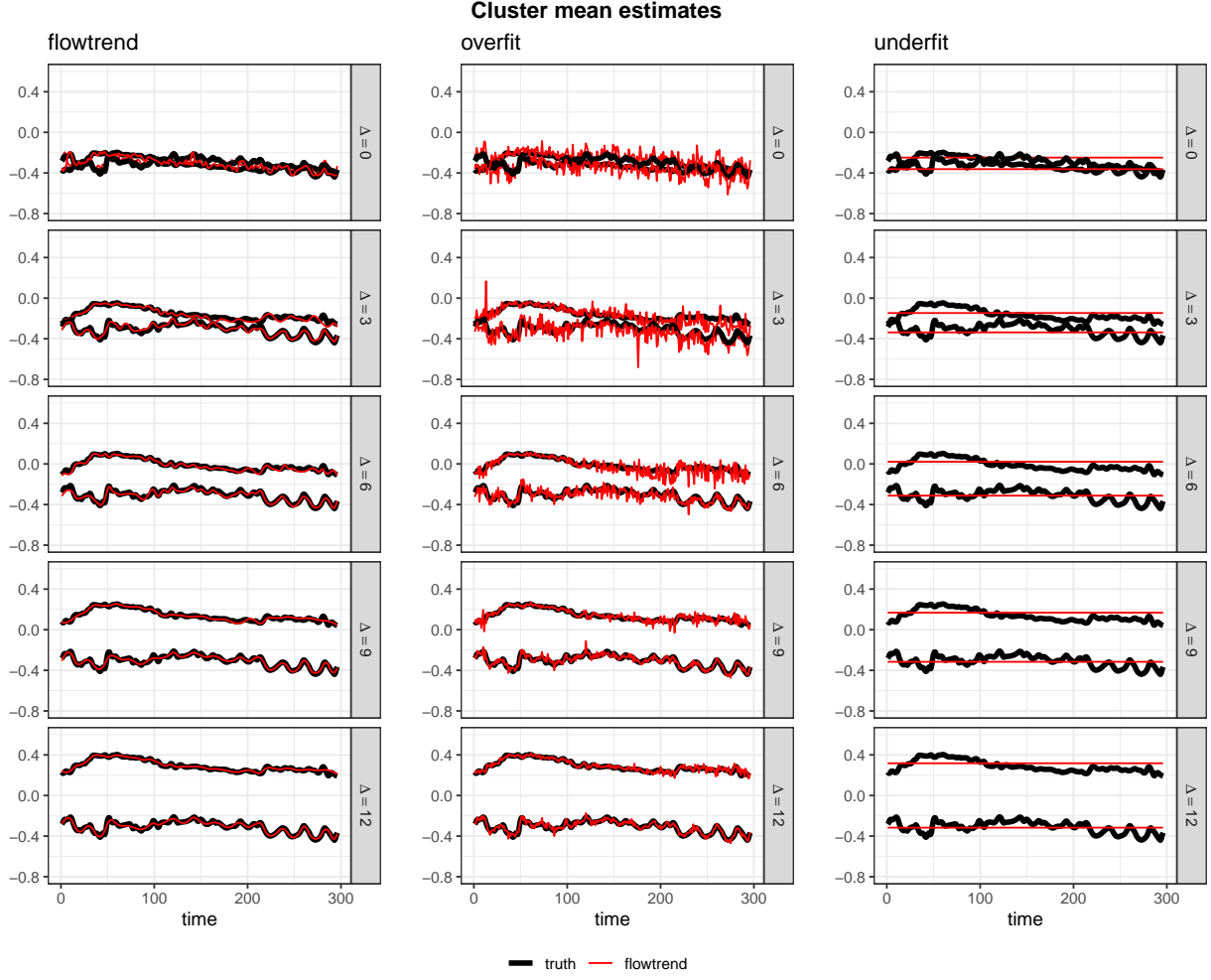


Figure 8: Cluster mean estimates from simulated datasets described in Section 3 are shown here. Each column of panels shows the estimates from the same model, over several signal sizes. The mean estimates by our proposed flowtrend model are the most accurate, over all signal sizes.

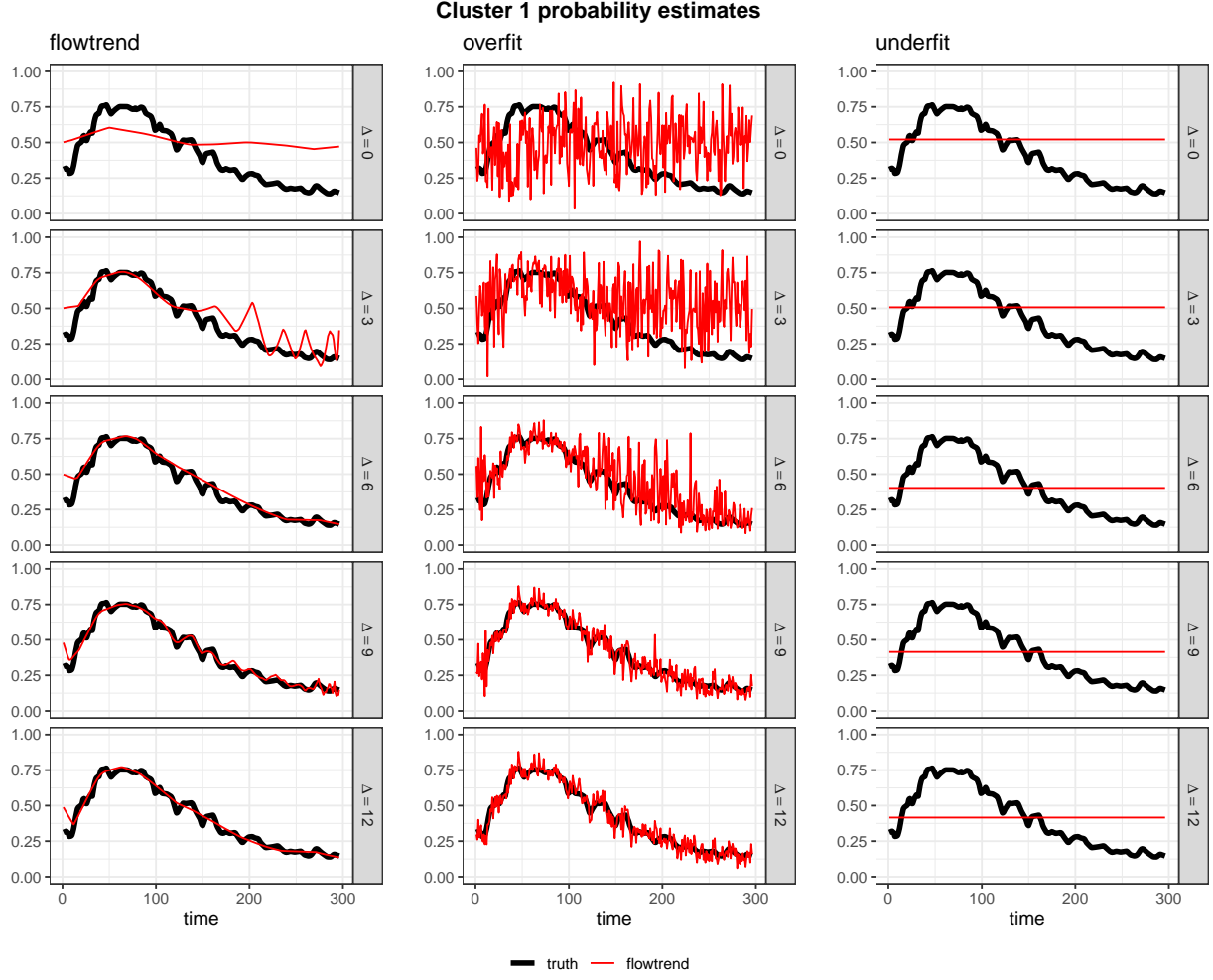


Figure 9: The probability estimates for one of the two clusters from simulated datasets described in Section 3 are shown here. Each column of panels shows the estimates from the same model, over several signal sizes. The other cluster's estimates are omitted because they are redundant. The probability estimates by our proposed flowtrend model are the most accurate, over all signal sizes.

Appendix B: ADMM Details

For a specific cluster k , the ADMM algorithm minimizes over each of the variables $\mu_{k..}, w, z, \{u_w^{(j)}\}_1^d$, and $\{u_z^{(t)}\}_1^T$ in the augmented Lagrangian:

$$\begin{aligned} L(\mu_{k..}, w, z, \{u_w^{(j)}\}_1^d, \{u_z^{(t)}\}_1^T) = & \frac{1}{2N} \sum_{t=1}^T \sum_{i=1}^{n_t} \tilde{\gamma}_{itk} (y_i^{(t)} - \mu_{kt.})^\top \hat{\Sigma}_k^{-1} (y_i^{(t)} - \mu_{kt.}) \\ & + \lambda_\mu \sum_{j=1}^d \|D^{(1)} w_{.j}\|_1 + \sum_{t=1}^T \mathbb{1}_\infty(\|z_{t.}\|_2 \leq r) \\ & + \sum_{t=1}^T \left[u_z^{(t)\top} (\mu_{kt.} - \bar{\mu}^{(k)} - z_{t.}) + \frac{\rho}{2} \|\mu_{kt.} - \bar{\mu}^{(k)} - z_{t.}\|^2 \right] \\ & + \sum_{j=1}^d \left[u_w^{(j)\top} (D^{(l_\mu)} \mu_{k.j} - w_{.j}) + \frac{\rho}{2} \|D^{(l_\mu)} \mu_{k.j} - w_{.j}\|^2 \right]. \end{aligned}$$

We provide details of the ADMM algorithm next.

1. $\mu_{k..} \leftarrow \operatorname{argmin}_{\mu_{k..}} L(\mu_{k..}, w, z, \{u_w^{(j)}\}_1^d, \{u_z^{(t)}\}_1^T)$

To start, let η denote the $d \times T$ matrix $\mu_{k..}^\top$ for cluster k . Then, we will rewrite several of the quantities in the augmented Lagrangian η . Let e_c denote a vector that has 1 in the c -th entry and 0 elsewhere. Then we write $\mu_{kt.}$ as $\eta e_t \in \mathbb{R}^{d \times 1}$, the time-wise average $\bar{\mu}^{(k)}$ as $\frac{1}{T} \eta \mathbb{1}_T \in \mathbb{R}^{d \times 1}$, and $\mu_{k.j}^\top$ as $e_j^\top \eta \in \mathbb{R}^{T \times 1}$, so that our minimization with respect to η is:

$$\begin{aligned} \eta \leftarrow \operatorname{argmin}_{\eta} & \frac{1}{2N} \sum_{t=1}^T \sum_{i=1}^{n_t} \tilde{\gamma}_{itk} (y_i^{(t)} - \eta e_t)^\top \hat{\Sigma}_k^{-1} (y_i^{(t)} - \eta e_t) \\ & + \sum_{t=1}^T \left[u_z^{(t)\top} (\eta e_t - \frac{1}{T} \eta \mathbb{1}_T - z_{t.}) + \frac{\rho}{2} \|\eta e_t - \frac{1}{T} \eta \mathbb{1}_T - z_{t.}\|^2 \right] \\ & + \sum_{j=1}^d \left[u_w^{(j)\top} (D^{(l_\mu)} \eta^\top e_j - w_{.j}) + \frac{\rho}{2} \|D^{(l_\mu)} \eta^\top e_j - w_{.j}\|^2 \right]. \end{aligned} \quad (18)$$

Now, we calculate the derivative of the objective in (18) with respect to η . We will examine one term at a time. The derivative of the first term is:

$$\begin{aligned} \frac{\partial}{\partial \eta} \left[\frac{1}{2N} \sum_{t=1}^T \sum_{i=1}^{n_t} \tilde{\gamma}_{itk} (y_i^{(t)} - \eta e_t)^\top \hat{\Sigma}_k^{-1} (y_i^{(t)} - \eta e_t) \right] &= \frac{1}{2N} \sum_{t=1}^T \sum_{i=1}^{n_t} \tilde{\gamma}_{itk} \frac{\partial}{\partial \eta} (y_i^{(t)} - \eta e_t)^\top \hat{\Sigma}_k^{-1} (y_i^{(t)} - \eta e_t) \\ &= \frac{1}{2N} \sum_{t=1}^T \sum_{i=1}^{n_t} -2 \tilde{\gamma}_{itk} \hat{\Sigma}_k^{-1} (y_i^{(t)} - \eta e_t) e_t^\top. \end{aligned}$$

The derivative of the second term is:

$$\begin{aligned} \frac{\partial}{\partial \eta} \sum_{t=1}^T & \left[u_z^{(t)\top} (\eta e_t - \frac{1}{T} \eta \mathbb{1}_T - z_{t.}) + \frac{\rho}{2} \|\eta e_t - \frac{1}{T} \eta \mathbb{1}_T - z_{t.}\|^2 \right] \\ &= \sum_{t=1}^T \frac{\partial}{\partial \eta} \left[u_z^{(t)\top} (\eta [e_t - \frac{1}{T} \mathbb{1}_T] - z_{t.}) + \frac{\rho}{2} \|\eta [e_t - \frac{1}{T} \mathbb{1}_T] - z_{t.}\|^2 \right] \\ &= \sum_{t=1}^T \left[u_z^{(t)\top} [e_t - \frac{1}{T} \mathbb{1}_T]^\top - \rho [\eta [e_t - \frac{1}{T} \mathbb{1}_T] - z_{t.}] [e_t - \frac{1}{T} \mathbb{1}_T]^\top \right]. \end{aligned}$$

Lastly, the third term can be rearranged using:

$$u_w^{(j)\top} (D^{(l_\mu)} \eta^\top e_j - w_{\cdot j}) = e_j^\top \eta (D^{(l_\mu)})^\top u_w^{(j)} - w_{\cdot j}^\top u_w^{(j)},$$

and

$$\|D^{(l_\mu)} \eta^\top e_j - w_{\cdot j}\|_2^2 = \text{Trace} \left[\left(e_j^\top \eta (D^{(l_\mu)})^\top - w_{\cdot j}^\top \right) \left(e_j^\top \eta (D^{(l_\mu)})^\top - w_{\cdot j}^\top \right)^\top \right].$$

which uses that $\|x\|_2^2 = \|x^\top\|_F = \text{Trace}(xx^\top)$. So, the derivative of the third term is:

$$\begin{aligned} \frac{\partial}{\partial \eta} \sum_{j=1}^d & \left[u_w^{(j)\top} (D^{(l_\mu)} \eta^\top e_j - w_{\cdot j}) + \frac{\rho}{2} \|D^{(l_\mu)} \eta^\top e_j - w_{\cdot j}\|^2 \right] \\ &= \frac{\partial}{\partial \eta} \sum_{j=1}^d \left[e_j^\top \eta (D^{(l_\mu)})^\top u_w^{(j)} - w_{\cdot j}^\top u_w^{(j)} + \frac{\rho}{2} \|e_j^\top \eta (D^{(l_\mu)})^\top - w_{\cdot j}^\top\|^2 \right] \\ &= \sum_{j=1}^d \left[e_j (u_w^{(j)})^\top D^{(l_\mu)} + \rho e_j \left(e_j^\top \eta (D^{(l_\mu)})^\top - w_{\cdot j}^\top \right) D^{(l_\mu)} \right]. \end{aligned}$$

Combining these, the overall derivative of the augmented Lagrangian with respect to η is:

$$\begin{aligned} & -\frac{1}{N} \sum_{t=1}^T \sum_{i=1}^{n_t} \tilde{\gamma}_{itk} \hat{\Sigma}_k^{-1} (y_i^{(t)} - \eta e_t) e_t^\top \\ & + \sum_{t=1}^T \left[u_z^{(t)} [e_t - \frac{1}{T} \mathbf{1}_T]^\top - \rho [\eta [e_t - \frac{1}{T} \mathbf{1}_T] - z_t] [e_t - \frac{1}{T} \mathbf{1}_T]^\top \right] \\ & + \sum_{j=1}^d \left[e_j (u_w^{(j)})^\top D^{(l_\mu)} + \rho e_j \left(e_j^\top \eta (D^{(l_\mu)})^\top - w_{\cdot j}^\top \right) D^{(l_\mu)} \right]. \end{aligned} \quad (19)$$

We set this derivative (19) equal to zero to get a matrix equation of the form:

$$A\eta B + \eta C + E = 0,$$

for matrices A, B, C and E defined as:

$$\begin{aligned} A &= \frac{1}{N} \hat{\Sigma}_k^{-1} \\ B &= \text{diag}(\{\tilde{\gamma}_{tk}\}_{t=1}^T) \\ C &= \rho \left[(D^{(l_\mu)})^\top D^{(l_\mu)} + \sum_{t=1}^T \tilde{e}_t \tilde{e}_t^\top \right] \\ E &= \frac{1}{N} \sum_{t=1}^T \sum_{i=1}^{n_t} \tilde{\gamma}_{itk} \hat{\Sigma}_k^{-1} y_i^{(t)} e_t^\top - \sum_{t=1}^T (u_z^{(t)} - \rho z_t) \tilde{e}_t^\top - \sum_{j=1}^d \left[e_j (u_w^{(j)})^\top D^{(l_\mu)} - \rho e_j w_{\cdot j}^\top D^{(l_\mu)} \right]. \end{aligned}$$

Each term's derivation is explained next. Matrix E is formed from the terms in (19) with no η :

$$-\frac{1}{N} \sum_{t=1}^T \sum_{i=1}^{n_t} \tilde{\gamma}_{itk} \hat{\Sigma}_k^{-1} y_i^{(t)} e_t^\top + \sum_{t=1}^T (u_z^{(t)} - \rho z_t) \tilde{e}_t^\top + \sum_{j=1}^d \left[e_j (u_w^{(j)})^\top D^{(l_\mu)} - \rho e_j w_{\cdot j}^\top D^{(l_\mu)} \right]. \quad (20)$$

where we have written $\tilde{e}_t^\top := [e_t - \frac{1}{T} \mathbf{1}_T]^\top$. Next, matrix C is formed by collecting the following two terms from (19):

$$\eta \cdot \rho \sum_{t=1}^T \tilde{e}_t \tilde{e}_t^\top + \sum_{j=1}^d \rho e_j e_j^\top \eta \rho (D^{(l_\mu)})^\top D^{(l_\mu)}, \quad (21)$$

and simplifying to

$$\eta \cdot \left(\rho \sum_{t=1}^T \tilde{e}_t \tilde{e}_t^\top + \rho (D^{(l_\mu)})^\top D^{(l_\mu)} \right) =: \eta C.$$

Lastly, A and B are formed by gathering the remaining term:

$$\frac{1}{N} \hat{\Sigma}_k^{-1} \eta \sum_{t=1}^T \sum_{i=1}^{n_t} \tilde{\gamma}_{itk} e_t e_t^\top,$$

which simplifies using $\tilde{\gamma}_{tk} = \sum_i \tilde{\gamma}_{itk}$ to

$$\frac{1}{N} \hat{\Sigma}_k^{-1} \cdot \eta \cdot \text{diag}(\{\tilde{\gamma}_{tk}\}_{t=1}^T) =: A \eta B.$$

Notice that B^{-1} can be right-multiplied to get:

$$A \cdot \eta + \eta \cdot C B^{-1} + E B^{-1} = 0, \quad (22)$$

where $B^{-1} = \text{diag}(\{\frac{1}{\tilde{\gamma}_{tk}}\}_{t=1}^T)$. This rearrangement to derive the Sylvester equation in (22) pays off since we can now solve it using a fast solver. One such solver can be found in the LAPACK library in C++. Furthermore, we can take advantage of that the matrices A and $C B^{-1}$ do not change across ADMM iterations, so that they can be Schur-decomposed and solved using an even faster Sylvester equation solver (e.g. Bartels-Stewart) that only uses triangular matrices as coefficients to a Sylvester equation. The solution of (22), transposed, is used to update $\mu_{k\cdot\cdot}$.

- 2a. $z_{t\cdot} \leftarrow \text{argmin}_{z_{t\cdot}} L(\mu_{k\cdot\cdot}, w, z, \{u_w^{(j)}\}_1^d, \{u_z^{(t)}\}_1^T)$ for $t = 1, \dots, T$

This update is similar to the update from Hyun et al. (2023), namely projecting the current parameter estimates and the auxillary variables onto the ball of radius r . Specifically,

$$z_{t\cdot} \leftarrow \begin{cases} \mu_{kt\cdot} - \bar{\mu}^{(k)} + u_z^{(t)}/\rho & \text{if } \|\mu_{kt\cdot} - \bar{\mu}^{(k)} + u_z^{(t)}/\rho\|_2 \leq r \\ r \frac{\mu_{kt\cdot} - \bar{\mu}^{(k)} + u_z^{(t)}/\rho}{\|\mu_{kt\cdot} - \bar{\mu}^{(k)} + u_z^{(t)}/\rho\|_2} & \text{otherwise} \end{cases}.$$

- 2b. $w_{\cdot j} \leftarrow \text{argmin}_{w_{\cdot j}} L(\mu_{k\cdot\cdot}, w, z, \{u_w^{(j)}\}_1^d, \{u_z^{(t)}\}_1^T)$ for $j = 1, \dots, d$

This update is inspired by Ramdas and Tibshirani (2016). Take the minimization with respect to $w_{\cdot j}$:

$$w_{\cdot j} \leftarrow \text{argmin}_{w_{\cdot j}} \sum_{i=1}^d \left[u_w^{(i)\top} (D^{(l_\mu)} \mu_{k\cdot i} - w_i) + \frac{\rho}{2} \|D^{(l_\mu)} \mu_{k\cdot i} - w_i\|^2 + \lambda_\mu \|D^{(1)} w_i\|_1 \right]. \quad (23)$$

This can be re-written as a *scaled* problem by completing the square. In particular, let $\epsilon_j = D^{(l_\mu)} \mu_{k\cdot j} - w_{\cdot j}$. The objective in (23) can be written as:

$$\begin{aligned} u_w^{(i)\top} \epsilon_i + \frac{\rho}{2} \|\epsilon_i\|^2 + \lambda_\mu \|D^{(1)} w_i\|_1 &= u_w^{(i)\top} \epsilon_i + \|\sqrt{\rho/2} \epsilon_i\|^2 + \lambda_\mu \|D^{(1)} w_i\|_1 \\ &= \frac{2}{2\sqrt{\rho/2}} u_w^{(i)\top} \sqrt{\rho/2} \epsilon_i + \|\sqrt{\rho/2} \epsilon_i\|^2 + \lambda_\mu \|D^{(1)} w_i\|_1 \\ &= \frac{2}{\sqrt{2\rho}} u_w^{(i)\top} \sqrt{\rho/2} \epsilon_i + \|\sqrt{\rho/2} \epsilon_i\|^2 + \lambda_\mu \|D^{(1)} w_i\|_1 \\ &= \left\| \sqrt{\rho/2} \epsilon_i + \frac{1}{\sqrt{2\rho}} u_w^{(i)} \right\|^2 + \lambda_\mu \|D^{(1)} w_i\|_1 - \frac{1}{2\rho} \|u_w^{(i)}\|^2 \end{aligned}$$

leading to the following minimization, after substituting back in ϵ :

$$w_{\cdot j} \leftarrow \text{argmin}_{w_{\cdot j}} \sum_{i=1}^d \left[\frac{\rho}{2} \|D^{(l_\mu)} \mu_{k\cdot i} - w_i\|^2 + \frac{1}{\rho} \|u_w^{(i)}\|^2 - \frac{1}{2\rho} \|u_w^{(i)}\|^2 + \lambda_\mu \|D^{(1)} w_i\|_1 \right].$$

Introducing the pseudo-response $\xi_j = D^{(l_\mu)} \mu_{k \cdot j} + \frac{1}{\rho} u_w^{(j)} \in \mathbb{R}^T$, we see that the above is equivalent to the problem

$$w_{\cdot j} \leftarrow \operatorname{argmin}_{w_{\cdot j}} \sum_{i=1}^d \left[\frac{\rho}{2} \|\xi_i - w_i\|^2 + \lambda_\mu \|D^{(1)} w_i\|_1 \right].$$

Note that each $w_{\cdot j}$ can be optimized separately, so the above is equivalent to fitting d fused-lasso problems, for which there exist efficient dynamic programming algorithms, such as the algorithm proposed in Johnson (2013). In practice, this means we solve d versions of the following problem:

$$\min_{w_{\cdot j}} \frac{\rho}{2} \|\xi_j - w_{\cdot j}\|^2 + \lambda_\mu \|D^{(1)} w_{\cdot j}\|_1 \iff \min_{w_{\cdot j}} \|\xi_j - w_{\cdot j}\|^2 + \frac{2\lambda}{\rho} \|D^{(1)} w_{\cdot j}\|_1.$$

$$3a. \quad u_z^{(t)} \leftarrow u_z^{(t)} + \rho(\mu_{kt} - \bar{\mu}^{(k)} - z_t) \text{ for } t = 1, \dots, T$$

$$3b. \quad u_w^{(j)} \leftarrow u_w^{(j)} + \rho(D^{(l_\mu)} \mu_{k \cdot j} - w_{\cdot j}) \text{ for } j = 1, \dots, d.$$

Steps 1 through 3b are repeated until the objective value numerically stabilizes.

Appendix C: Lemma 2 from Tibshirani (2014)

Here, we reproduce Lemma 2 in Section 3.3 from a manuscript on trend filtering (Tibshirani, 2014), where the authors write as follows. We can transform the trend filtering problem in

$$\hat{\beta} = \operatorname{argmin}_{\beta \in \mathbb{R}^n} \frac{1}{2} \|y - \beta\|_2^2 + \frac{n^k}{k!} \lambda \|D^{(k+1)} \beta\|_1,$$

into lasso form, just like the representation for locally adaptive regression splines in Lemma 1 (not reproduced for brevity).

Lemma 2. The trend filtering problem above is equivalent to the lasso problem:

$$\hat{\alpha} = \operatorname{argmin}_{\alpha \in \mathbb{R}^n} \frac{1}{2} \|y - H\alpha\|_2^2 + \lambda \sum_{j=k+2}^n |\alpha_j|$$

in that the solutions satisfy $\hat{\beta} = H\hat{\alpha}$. Here, the predictor matrix $H \in \mathbb{R}^{n \times n}$ is given by

$$H_{ij} = \begin{cases} i^{j-1}/n^{j-1} & \text{for } i = 1, \dots, n, j = 1, \dots, k+1, \\ 0 & \text{for } i \leq j-1, j \geq k+2 \\ \sigma_{i-j+1}^{(k)} \cdot k!/n^k & \text{for } i > j-1, j \geq k+2 \end{cases}$$

where we define $\sigma_i^{(0)} = 1$ for all i and

$$\sigma_i^{(k)} = \sum_{j=1}^i \sigma_j^{(k-1)} \text{ for } k = 1, 2, 3, \dots,$$

i.e., $\sigma_i^{(k)}$ is the k th order cumulative sum of $(1, 1, \dots, 1) \in \mathbb{R}^i$.

References

- Aghaeepour, N. (2010). Flowmeans: non-parametric flow cytometry data gating. *R package version*, 1(0).
 Arnold, T., Sadhanala, V., and Tibshirani, R. J. (2014). glmgen: Fast generalized lasso solver.

- Arnold, T. B., Tibshirani, R. J., Arnold, M. T., and ByteCompile, T. (2020). Package ‘genlasso’. *Statistics*, 39(3):1335–1371.
- Bien, J. and Vossler, P. (2023). *litr: Literate Programming for Writing R Packages*. R package version 0.9.1.
- Boyd, S., Parikh, N., Chu, E., Peleato, B., and Eckstein, J. (2011). Distributed optimization and statistical learning via the alternating direction method of multipliers. *Foundations and Trends® in Machine Learning*, 3(1):1–122.
- Cheung, M., Campbell, J. J., Whitby, L., Thomas, R. J., Braybrook, J., and Petzing, J. (2021). Current trends in flow cytometry automated data analysis software. *Cytometry Part A*, 99(10):1007–1021.
- Dempster, A. P., Laird, N. M., and Rubin, D. B. (1977). Maximum likelihood from incomplete data via the em algorithm. *Journal of the Royal Statistical Society Series B: Statistical Methodology*, 39(1):1–22.
- Dubelaar, G. B., Gerritzen, P. L., Beeker, A. E., Jonker, R. R., and Tangen, K. (1999). Design and first results of CytoBuoy: a wireless flow cytometer for in situ analysis of marine and fresh waters. *Cytometry*, 37(4):247–254.
- Friedman, J., Hastie, T., Tibshirani, R., Narasimhan, B., Tay, K., Simon, N., and Qian, J. (2022). Package ‘glmnet’. *Journal of Statistical Software*. 2010a, 33(1).
- Ge, Y. and Sealfon, S. C. (2012). flowpeaks: a fast unsupervised clustering for flow cytometry data via k-means and density peak finding. *Bioinformatics*, 28(15):2052–2058.
- Huang, M., Li, R., and Wang, S. (2013). Nonparametric mixture of regression models. *Journal of the American Statistical Association*, 108(503):929–941.
- Hyun, S., Rolf Cape, M., Ribalet, F., and Bien, J. (2023). Modeling cell populations measured by flow cytometry with covariates using sparse mixture of regressions. *The Annals of Applied Statistics*, 17(1).
- Johnson, N. A. (2013). A dynamic programming algorithm for the fused lasso and l0-segmentation. *Journal of Computational and Graphical Statistics*, 22(2):246–260.
- Kim, S.-J., Koh, K., Boyd, S., and Gorinevsky, D. (2009). ℓ_1 trend filtering. *SIAM review*, 51(2):339–360.
- Knuth, D. E. (1992). *Literate Programming*. Center for the Study of Language and Information Publication Lecture Notes. Centre for the Study of Language & Information, Stanford, CA.
- Kuhn, H. W. (1955). The hungarian method for the assignment problem. *Naval research logistics quarterly*, 2(1-2):83–97.
- Malek, M., Taghiyar, M. J., Chong, L., Finak, G., Gottardo, R., and Brinkman, R. R. (2014). flowdensity: reproducing manual gating of flow cytometry data by automated density-based cell population identification. *Bioinformatics*, 31(4):606–607.
- Minoura, K., Abe, K., Maeda, Y., Nishikawa, H., and Shimamura, T. (2019). Model-based cell clustering and population tracking for time-series flow cytometry data. *BMC Bioinformatics*, 20(S23).
- Olson, R. J., Shalapyonok, A., and Sosik, H. M. (2003). An automated submersible flow cytometer for analyzing pico- and nanophytoplankton: Flowcytobot. *Deep Sea Research Part I: Oceanographic Research Papers*, 50(2):301–315.
- Quintelier, K., Couckuyt, A., Emmaneel, A., Aerts, J., Saeys, Y., and Van Gassen, S. (2021). Analyzing high-dimensional cytometry data using flowsom. *Nature Protocols*, 16(8):3775–3801.
- Ramdas, A. and Tibshirani, R. J. (2016). Fast and flexible admm algorithms for trend filtering. *Journal of Computational and Graphical Statistics*, 25(3):839–858.
- Rand, W. M. (1971). Objective criteria for the evaluation of clustering methods. *Journal of the American Statistical Association*, 66(336):846–850.